Research paper

Robust visible/near-infrared light driven hydrogen generation over Z-scheme conjugated polymer/CdS hybrid

Xiaohu Zhang, Jie Xiao, Min Hou, Yonggang Xiang, Hao Chen*

College of Science, Huazhong Agricultural University, Wuhan 430070, PR China

ABSTRACT

Direct Z-scheme organic/inorganic semiconductor hybrid is seldom reported for photocatalytic H_2 production from water splitting. Reported herein is a new type of organic/inorganic hybrid fabricated with modified conjugated polybenzothiadiazole (B-BT-1,4-E, noted as BE) flake and CdS nanorod. The internal Z-scheme electron transfer mechanism is evidenced by detecting the loading position of Pt through a in-situ photodeposition technique. It is found that the Z-scheme BE-CdS hybrid possesses broad visible/near-infrared (vis/NIR) light absorption region (400–700 nm) and rapid photogenerated e^-/h^+ separation rate. Photocatalytic performances reveal that the H_2 production rate of optimal cocatalyst-free BE-CdS hybrid is 8.3 and 23.3 times higher than that of CdS and BE respectively, and a high apparent quantum yield (AQY) of 7.5% at 420 nm is obtained over the hybrid catalyst. This work opens new opportunities for exploiting highly efficient solar water splitting performances.

1. Introduction

Solar hydrogen fuel is an ideal source of energy to solve the ever-increasing requirement of energy for the sustainable development of mankind [1–5]. Generally, the core of a solar hydrogen fuel production system is a semiconductor or metal-based molecule, among which semiconductor-based photocatalytic H_2 production procedure is always the main stream up to date. Numerous state-of-the-art semiconductors (including TiO_2, CdS, g-C_3N_4 etc.) have been investigated widely for a rather long time, but the development of photocatalytic H_2 production technology is still impeded sorely [5–10]. Either limited visible light absorption ability or slow photogenerated e^-/h^+ separation rate and most of the time is the combination of the two factors cause low solar-to-hydrogen conversion efficiency of most semiconductor alone.

Fabrication of semiconductor/semiconductor heterojunction or hybrid with favorable type II, *p-n* or Z-scheme energy band and electron transfer structure is one of the most efficient strategies to enormously extend the visible light absorption region and accelerate the e^-/h^+ separation of each semiconductors [2,11–14]. Among them, the redox potential of a heterojunction system can be maximized by Z-scheme concept because the reduction and oxidation processes occur on the semiconductor with the higher reduction and oxidation potentials. For instance, Zhang et al. fabricate a nonmetal plasmonic Z-scheme photocatalyst with $W_{18}O_{49}$/g-C_3N_4 heterostructure, which can generate long-lived active electrons for pohotocatalytic H_2 production [10]. Z-

scheme hierarchical g-C_3N_4-supported $CuInS_2$ is reported to improve photocarrier separation and enhance photocatalytic water splitting efficiency by Li et al. [15]. Zhou et al. reported $BiVO_4$ nanowires decorated with CdS nanoparticles as Z-scheme photocatalyst for efficient photocatalytic H_2 production [16]. However, the intrinsic energy band positions and the corresponding band-gap of most inorganic semiconductors cannot be altered easily due to their assured crystal and band component. In this regard, sole inorganic/inorganic semiconductor hybrid is unfavorable in terms of extending visible and near-infrared (NIR) light harvest. Of note, g-C_3N_4, as a hot organic semiconductor material, is also not a perfect candidate because of its rather wide band-gap (~2.7 eV) and limited visible light absorption region (λ < 450 nm) [5,17,18]. Conjugated polymer, an emerging class of organic semiconductor and mostly utilized in organic photovoltaic, have recently found their application in photocatalytic H_2 production from water under visible light irradiation [19,20]. For instance, Pati et al. reported an initial rate of hydrogen evolution up to 50 ± 0.5 mmol g^{-1} h^{-1} over a type of polymer-based Pdots and found that the N centre of the benzothiadiazole unit plays a crucial role in photocatalysis [21]. Chen et al. fabricate polymer heterojunctions between polyfluorene family polymers and g-C_3N_4 by molecular design, and an enhanced AQY of 27% at 440 nm over PCzF/g-C_3N_4 is obtained with 1.0 wt% Pt as cocatalyst [22]. In addition, photocatalytic H_2 production over conjugated polymers with planarized structure and design strategy of electron-donor-acceptor were also reported by Sprick
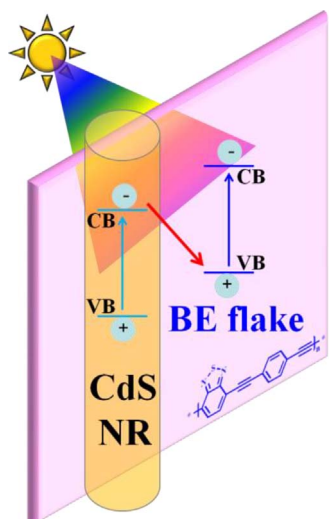
Fig. 1. Confguration of energy band positions and Z-scheme photogenerated charge carriers transfer in the BE-CdS hybrid photocatalyst under visible light irradiation.

and Yang et al. respectively [23,24]. The chemical structure, color, band-gap and energy band position of conjugated polymers can be conventionally tuned by varying raw materials and different polymerization procedures. Very recently, B-BT-1,4-E, a new modified conjugated polybenzothiadiazole polymer, is reported by our group to be an efficient noble-metal-free organic semiconductor catalyst for photocatalytic H_2 production, but the solar-to-hydrogen conversion efficiency need to be further improved [25]. However, this new type of conjugated polymer has never been reported to fabricated Z-scheme hybrid with an inorganic semiconductor for photocatalytic H_2 production as our known.

Herein, energy band engineering between inorganic semiconductor (CdS) and conjugated polymer (B-BT-1,4-E, noted as BE) is deliberately utilized to fabricated new type of organic/inorganic hybrid photocatalyst based on their matched energy band levels. And a direct Z-scheme mechanism (see Fig. 1) for enhanced e^-/h^+ separation is proposed and confirmed by detecting the Pt loading position through in-situ photodeposition method. Simultaneously, the BE-CdS hybrid can absorb broad Vis/NIR light region from 400 to 700 nm, which combines the characteristic light absorption ability of both BE and CdS. Finally, extraordinarily high visible-light-driven photocatalytic H_2 production activity from water reduction is observed on the bi-functional Z-scheme BE-CdS hybrid photocatalyst because of its broad light absorption and accelerative e^-/h^+ separation.

2. Experimental section

2.1. Catalyst preparation

B-BT-1,4-E (BE) is synthesized by ourself conventionally by Sonogashira–Hagihara cross-coupling polycondensation following our previous report [25]. CdS nanorods were synthesized through a solvothermal reaction of $CdCl_2 \cdot 2 \cdot 5H_2O$ and NH_2CSNH_2 [26]. The BE-CdS-x hybrid, where x represent the ratio of BE to CdS (w/w), was fabricated by in-situ polycondensation of BE in the presence of CdS. Take BE-CdS-3.3 as example, a dry 250 mL round-bottom flask was charged with CdS (300 mg), 4,7-dibromobenzo[c-1,2,5]thiadiazole (11.4 mg) and 1,4-diethynylbenzene (4.9 mg), $Pd(PPh_3)Cl_2$, CuI and 80 mL mixed solvent (DMF/TEA = 1/1), and then the resulting mixture was stirred at 80 °C for 24 h under Ar condition. After that, the precipitate was collected by filtration, and the solid was washed with methanol and CH_2Cl_2 for 48 h. The final product was dried at 60 °C overnight. For other BE-CdS-x hybrid, the amount of materials were changed accordingly except for CdS nanorod.

2.2. Characterization

The XRD patterns were recorded on an powder X-ray diffractometer with Cu Ka radiation (D8 Advance Bruker Inc., Germany). Raman spectroscopy was conducted using a microscopic confocal Renishaw 1000 NR Raman spectrometer. The morphology was analyzed using TEM on a JEOL JEM-2010 and a Tecnai G2 F20 S-TWIN. X-ray photoelectron spectroscopy (XPS) was measured on a Thermo Fisher ESCALAB 250Xi X-ray photoelectron spectroscope equipped with Al Kα radiation operated at 200 W. The Fourier transform infrared spectra (FTIR) of the samples were recorded using a Nicolet iS50FT-IR spectrometer (Thermo, USA). The Brunauer–Emmett–Teller (BET) specific surface area was evaluated using a nitrogen adsorption–desorption apparatus (ASAP 2040, Micrometrics Inc., USA) with all samples degassed at 120 °C for 12 h prior to measurements. UV–vis diffuse reflectance spectra were obtained for the dry-pressed disk samples using a Shimadzu UV-3100 recording spectrophotometer equipped with an integrating sphere. PL measurements were conducted with a fluorescence spectrometer (F-4600, Hitachi Inc., Japan) at room temperature with excitation wavelength 340 nm.

2.3. Measurement of photocatalytic activity

A top-irradiation reaction vessel connected to a closed gas system is adopted to carry out the photocatalytic H_2 production activity. Typically, 30 mg catalyst was dispersed in 30 mL equivalent Na_2S/Na_2SO_3 aqueous solution, and irradiated under $\lambda > 420$ nm by a 300 W Xe-lamp (PLS SXE300, Beijing Perfectlight Inc., China) equiped with a cutoff filter ($\lambda > 420$ nm) or band-pass filters ($\lambda = 420$, 500 nm etc.) after thoroughly removing air. For Pt loaded samples, calculated amount of H_2PtCl_6 was added into the suspension before irradiation. The H_2 production rate was tested by a GC (SP7820, TCD detector, 5 Å molecular sieve columns, and Ar carrier).

The apparent quantum yield (AQY) for photocatalytic H_2 production was calculated as follows [25]:

$$AQY(\%) = \frac{2 \times \text{Number of evolved } H_2 \text{ molecules}}{\text{Number of incident photons}} \times 100\%$$

The number of incident photons is measured by a calibrated Si photodiode (SRC-1000-TC-QZ-N, Oriel, USA), and the distance between the calibrated Si photodiode and Xe-lamp with different filters is 10 cm.

2.4. Photoelectrochemical measurements

The photocurrent and electrochemical impedance measurement were performed on a CHI 660D electrochemical work station (Chenhua Instrument, Shanghai, China) in a conventional three electrode configuration with Pt foil as the counter electrode and Ag/AgCl (saturated KCl) as the reference electrode. 0.1 M Na_2SO_4 aqueous solution was used as the electrolyte. The working electrodes were prepared as follows: 10 mg of the prepared photocatalyst and 0.5 mL Nafion dispersing reagent were added into 5 mL absolute ethyl alcohol and sonicated for 30 min. The resulting slurry was then spread on a 2.5 × 1.0 cm indium–tin oxide (ITO) glass substrate and dried in air. In addition, a 300 W Xe lamp (PLS SXE300, Beijing Perfectlight Inc., China) was utilized as the light source ($\lambda > 420$ nm) during the photocurrent measurement.

3. Results and discussion

3.1. Crystal phase and microstructure analyses

The morphologic and crystalline properties of the hybrid are illustrated by XRD and TEM patterns shown in Figs. 2 and 3. As can be seen in Fig. 2, CdS exhibits high quality of crystallinity because of its sharp diffraction peaks, corresponding to hexagonal phase (PDF#77-2306).
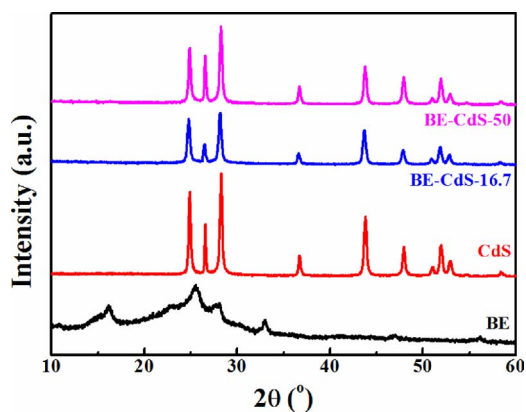
Fig. 2. XRD patterns of BE, CdS and BE-CdS hybrid.

Fig. 4. DRS spectra of BE, CdS and BE-CdS hybrid.

And BE is found to be amorphous with broad and low peaks, which is the common character of most conjugated polymers [23,24,27]. In addition, BE-CdS hybrid can only show XRD peaks as same as that of CdS even with very high relative proportion of BE (BE-CdS-50.0), which should be caused by the very strong diffraction peaks of CdS and amorphous of BE. Fig. S1 gives the TEM images of CdS and BE alone. Obviously, CdS and BE mainly show nanorod and agglomerate flake morphology respectively. HRTEM images of CdS and BE-CdS hybrid in Fig. 3 give assured information. Fig. 3a further confirms the prepared nanorod is CdS with lattice spacing of ~0.336 nm, corresponding to (002) plane [28]. Fig. 3b show the HRTEM of BE-CdS hybrid, in which the amorphous property of BE is confirmed clearly. Additionally, the interpenetration and interleaving between BE and CdS can be observed, indicating intimate contact occurs in the hybrid photocatalyst. The FTIR and Raman spectra of BE-CdS hybrid (see Fig. S2 in the Supporting Information) also exhibit the combination of BE and CdS. The N_2 adsorption–desorption isotherm (see Fig. S3 in the Supporting Information) indicates the slight change of Brunauer–Emmett–Teller (BET) surface areas between hybrid and alone materials may not the reason for the enhancement of photocatalytic performance in the following section.

3.2. Light absorption and Z-scheme photogenerated e^-/h^+ separation analyses

Visible light absorption ability of photocatalyst is the first and fundamental factor, which is investigated by solid state UV–vis diffuse reflectance spectra (DRS) and shown in Fig. 4. As revealed, CdS and BE can absorb visible light up to ~530 nm and 700 nm alone respectively. And the BE-CdS hybrid combines the characteristics of the two components and exhibits strong visible/NIR light absorption ability from 400 to 700 nm. That is, broad sola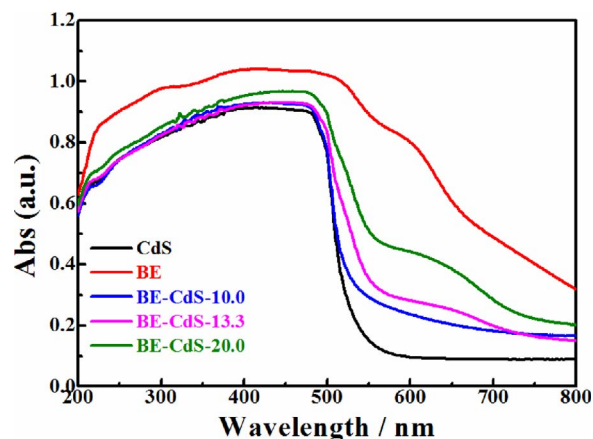r light region might be utilized to produce solar hydrogen with the present BE-CdS hybrid photocatalyst. Separation and migration of photogenerated e^-/h^+ after visible light excitation are decisive steps to the performance of a photocatalyst, and the unavoidable deactivation of e^-/h^+ inside or on the surface of catalyst is tremendously harmful [29]. For a semiconductor/semiconductor hybrid, the configuration of relative energy band positions is significantly important for the internal charge separation. Fig. S4 shows the band-gap (2.31 eV) and VB (1.75 eV) values of CdS based on its DRS absorption edge and XPS valence band spectrum measurement [30]. And then the CB value of CdS can be calculated as −0.56 eV. The CB and VB values of BE are found to be −0.69 and 0.95 eV respectively in our previous report [25]. Accordingly, favorable staggered energy band arrangement between CdS and BE is obtained, and then the separation of photoinduced e^-/h^+ can be accelerated significantly. This point can be confirmed by steady-state photoluminescence (PL), photocurrent-time and electrochemical impedance curves. As shown in Fig. 5, CdS and BE exhibit strong emission peaks at ~510 and 568 nm respectively because of their intrinsic excitation and the quick recombination of photogenerated e^-/h^+ pairs. However, the corresponding emission intensity of BE-CdS hybrid sharply drops to very low values, indicating the e^-/h^+ recombination of both CdS and BE are restrained efficiently, and internal charge separation happens on the BE-CdS hybrid [31,32]. As is well known, photocurrent-time test is a widely adopted technique to investigate the separation efficiency of e^-/h^+ under light irradiation. Fig. 6a reveals that the photocurrent values of BE-CdS hybrid is much higher than that of BE or CdS alone under visible light irradiation, implying that the formation of BE-CdS hybrid can significantly increase the available photogenerated charge carriers due to its quick internal charge separation, which will be favorable for a photocatalytic reaction [33,34]. As confirmed by the electrochemical impedance spectroscopy in Fig. 6b, BE-CdS hybrid exhibits considerably lower electrochemical
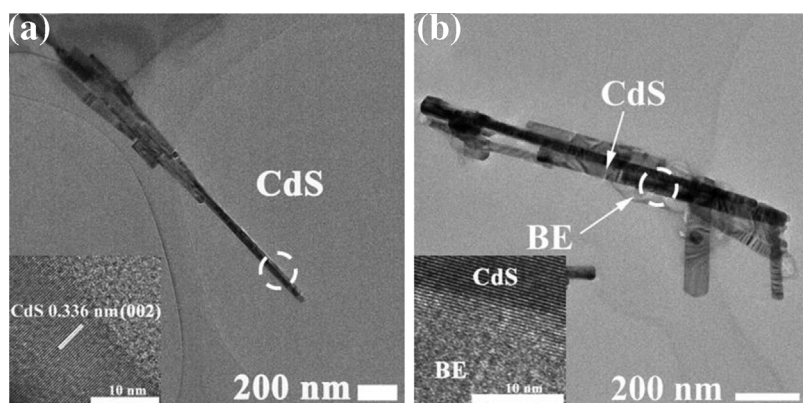

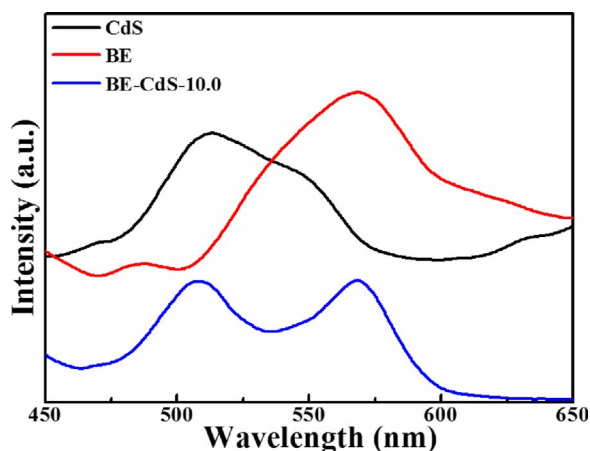Fig. 3. TEM and corresponding HRTEM image of CdS nanorod (a) and BE-CdS-10.0 hybrid (b).

Fig. 5. Steady-state PL spectra of BE, CdS and BE-CdS hybrid.

impedance value than that of either CdS or BE, that is, the transport of photoexcited electron is most favorable in the BE-CdS hybrid catalyst [29].

However, two different electron transfer modes, conventional type II (Fig. S5a) or Z-scheme (Fig. S5b), may happen based on the present staggered energy band arrangement, and all of the aforementioned tests cannot distinguish the two modes clearly. And then, a technique of in-situ photoreduction of Pt from H_2PtCl_6 is carried out to explore the assured electron transfer mechanism of the present BE-CdS hybrid [15]. Generally, Pt^{4+} in H_2PtCl_6 can be easily reduced to be Pt nanoparticles by photogenerated e^- under light irradiation in the present of semiconductor [18,34]. As confirmed by the HRTEM image of Fig. 7a and S6, Pt nanoparticles with clear characteristic lattice fringe corresponding to Pt(111) plane are loaded on BE flakes rather than CdS nanorod, implying the electron are transferred form CB of CdS to the VB of BE through Z-scheme mechanism rather than conventional type II mechanism with electron transfer from the CB of BE to the CB of CdS. To further confirm the value state of Pt after in-situ photoreduction procedure, the Pt XPS spectrum is tested and shown in Fig. 7b. The binding energy values of Pt $4f_{7/2}$ and $4f_{5/2}$ can be observed to be 72.3 and 75.5 eV, which are almost equal to the standard binding energy of Pt metal, suggesting that Pt exists as a metallic form in the nanocomposite [35].

3.3. Photocatalytic H_2 evolution activity

In light of the aforementioned broad visible/NIR light absorption ability and highly efficient Z-scheme internal electron separation of BE-CdS hybrid, photocatalytic water reduction for H_2 production of the hybrid photocatalyst is performed in the presence of equivalent Na_2S-Na_2SO_3 as sacrificial reagent under visible light irradiation ($\lambda > 420$ nm). Blank experiments reveal that no any H_2 is detected when there is no catalyst or light irradiation, indicating that the

production of H_2 from the present system is coming from the semi-conductor based photocatalytic procedure. Fig. 8a gives the comparison of visible light driven H_2 production activity of various catalyst. CdS, a well known semiconductor for water reduction [36,37], exhibits the H_2 production rate of 148.9 μmol/h alone without any co-catalyst addition. And BE has also been proven to be an efficient polymer photocatalyst [25] and the H_2 evolution rate of BE alone is 52.8 μmol/h without co-catalyst. For the BE-CdS-10.0 hybrid catalyst, it is amazing that the H_2 formation rate reaches to 1229.7 μmol/h, which is 8.3 and 23.3 times higher than that of CdS and BE respectively. Of note, a H_2 production rate of 183.3 μmol/h is obtained over BE-CdS-10.0 hybrid catalyst even under $\lambda > 600$ nm irradiation with a 600 nm cut-off filter, indicating the excellent near-infrared light responsiveness of the hybrid catalyst. The sharply improved photoactivity of the BE-CdS hybrid compared to BE and CdS should be attributed to the above analyzed broad visible/NIR light absorption ability and the internal Z-scheme quick electron transfer and separation rate. To confirm the irreplaceable importance of in-situ fabrication of the BE-CdS hybrid catalyst, H_2 production is carried out over a mechanical mixture of BE and CdS (noted as BE + CdS) by grinding appropriate amount of BE and CdS according to the proportion of BE-CdS-10.0. And as is proven by Fig. S7, the H_2 production rate is 243.6 μmol/h for (BE + CdS) catalyst, which is much lower than that of BE-CdS hybrid but rather higher than either BE or CdS. That is, the combination of BE and CdS can indeed improve the electron separation and transfer efficiency. Of note, Pd^{2+} must exist in the BE-CdS hybrid because of the residual Pd^{2+} during the palladium-catalyzed polycondensation procedure is ineluctable for BE and all of the reported conjugated polymers for H_2 production, and no efficient method has been reported to successfully remove the residual Pd^{2+} from the polymers [23–25,27]. To rule out whether the residual Pd^{2+} during the in-situ polymerization of BE can participate in the subsequent photocatalytic H_2 production procedure or not. The $Pd(PPh_3)_2Cl_2$-CdS is prepared by the same procedure in the absence of 4,7-dibromobenzo[c-1,2,5]thiadiazole and 1,4-diethylnylbenzene, and it exhibits a H_2 production rate of 210.5 μmol/h, which is also much lower than that of BE-CdS hybrid but slightly higher than the value of pure CdS, indicating that the effect of residual Pd^{2+} should be very finite. More importantly, it is found that the existence form of Pd^{2+} seems no change after a photocatalytic H_2 production procedure, which is detected by XPS curve and shown in Fig. S8. As can be evidenced, the peaks at ~336.6 and 341.9 eV for Pd^{2+} $3d_{5/2}$ and Pd^{2+} $3d_{3/2}$ binding energy shows no significant change when BE-CdS-10.0 hybrid suffers 3 h visible light irradiation for H_2 production [7,38]. That is to say, the residual Pd^{2+} cannot be reduced to Pd^0 metal as co-catalyst to improve the photoactivity of the present BE-CdS hybrid catalyst. Anyway, we try to further improve the photocatalytic H_2 production rate of the BE-CdS hybrid by introduction of Pt cocatalyst, which is the most known and efficient co-catalyst. Fig. S7 exhibits that H_2 production rate of 3006.0 μmol/h is observed when certain amount of H_2PtCl_6 (corresponding to 1.0 wt% Pt if all of the Pt^{4+} can be photoreduced) is added to the catalyst suspension before irradiation.
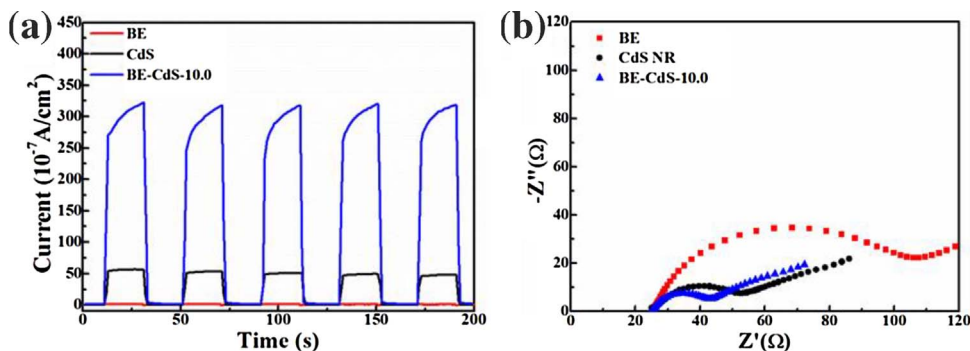

Fig. 6. Photocurrent-time behavior (a) and electrochemical impedance spectra (b) of BE, CdS and BE-CdS hybrid.
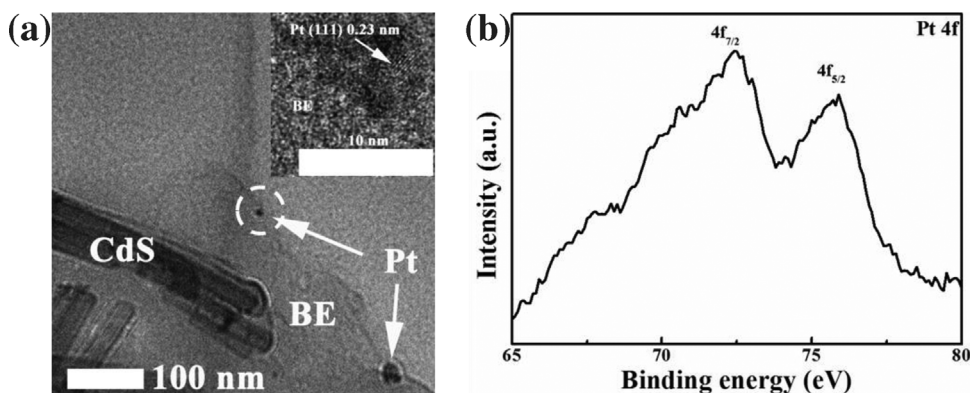
Fig. 7. (a) TEM and corresponding HRTEM images and (b) Pt XPS spectrum of BE-CdS-10.0 hybrid after in-situ photodeposition of Pt from H_2PtCl_6.

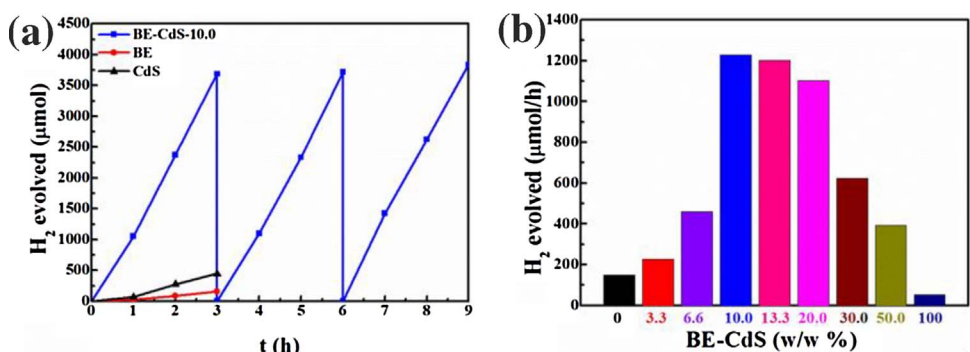**Fig. 8.** (a) Comparison of H_2 production activity of BE, CdS and BE-CdS hybrid under visible light irradiation. (b) Effect of BE amount on the H_2 production rate of BE-CdS hybrid, in which 0 and 100 represent pure CdS and BE respectively. Reaction conditions: 30 mg catalysts are suspended in 30 mL 0.25 M Na_2S/Na_2SO_3 aqueous solution and a 300 W Xe-lamp equipped with a 420 nm cut-off flitter is used as light source.

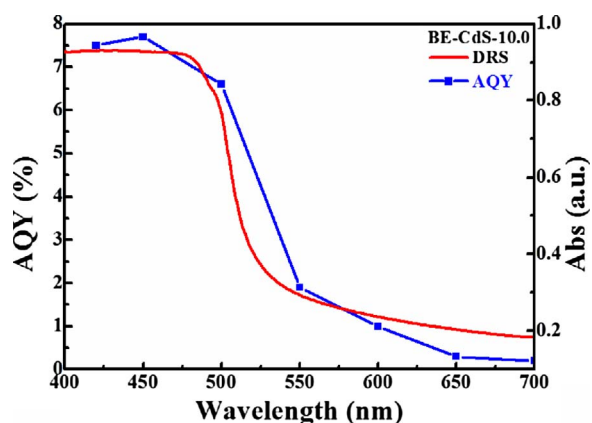**Fig. 9.** Wavelength dependent AQY values of BE-CdS-10.0 hybrid. Reaction conditions: 30 mg catalysts are suspended in 30 mL 0.25 M Na_2S/Na_2SO_3 aqueous solution and a 300 W Xe-lamp equipped with series of band-pass flitters (420, 450, 500, 550, 600, 650 and 700 nm) is used as light source.

For a typical photocatalytic H_2 production procedure, the three main steps: light absorption, e^-/h^+ separation and surface redox reaction can all strongly affect its efficiency. On one hand, Fig. 4 reveals that the visible/NIR light absorption intensity and region of BE-CdS hybrid can be gradually extended with increasing the relative fraction of BE to CdS. On the other hand, the present Z-scheme electron transfer mode indicates that BE is the main H_2 production supporter, and the increasing amount of BE will be favorable for improving photoactivity. Indeed, the H_2 production rate increases incipiently as shown in Fig. 8b. For example, the H_2 evolution rate is 225.5 μmol/h with BE-CdS-3.3 as catalyst, but the value increases to be 459.4 and 1229.7 μmol/h when BE-CdS-6.6 and BE-CdS-10.0 are used as catalyst respectively. As can be seen in Fig. 8b, an optimal range of BE content is found to be from 10.0 to 20.0 w/w%, and then the H_2 production rate drops slowly when the BE amount is further increased. This phenomenon can be rationalized considering the e^-/h^+ separation aspect. For the present Z-scheme BE-

CdS hybrid, the quick internal electron transfer is based on appropriate BE and CdS combination, and the excitation of both BE and CdS should be optimal and sufficient. Excessive amount of BE will shade the available light absorption for CdS, and then affect the excitation and generation of e^-/h^+ pairs. In addition, the hydrophobicity of BE should be noted, which will also affect the photoactivity of BE-CdS hybrid with very high amount of BE. Except for the effect of the component of BE-CdS hybrid, the influence of concentration of catalyst and sacrificial reagent are investigated, as shown in Fig. S9. And the optimal photoreaction conditions are 1.0 g/L BE-CdS hybrid catalyst suspended in 0.25 M Na_2S/Na_2SO_3 aqueous solution. The H_2 evolution stability and cycle performance is shown in Fig. 8a over BE-CdS-10.0 catalyst, and no obvious decrease of H_2 production rate is observed in the tested runs. In addition, the stability of the hybrid after visible light irradiation is also further characterized by XRD, FTIR, DRS and Raman curves as shown in Fig. S10 and S11. It can be found that all of these curves of BE-CdS-10.0 catalyst after H_2 production show no obvious change compared with the original spectra, indicating the stability of catalyst.

3.4. AQY test and mechanism for the enhanced photoactivity

The wavelength dependent AQY values of BE-CdS-10.0 is given in Fig. 9, revealing the correspondence of its photoactivity for H_2 evolution with its absorption curve. A high AQY of 7.5% is obtained at 420 nm without cocatalyst, and the BE-CdS hybrid can work under the whole vis/NIR light region with an AQY of 0.2% even at 700 nm. The AQY values at 420 nm of series of catalyst is compared in Fig. S12, in where pure BE or CdS exhibits much lower AQY than that of BE-CdS hybrid and the AQY can be further improved to be 28.4% by adding of Pt cocatalyst. To compare with other works, some recent AQY values at 420 nm reported on CdS and conjugated polymers are listed in Table S1. As revealed, the AQY of the present BE-CdS hybrid without cocatalyst is lower than most CdS/co-catalyst system (of note, CdS is often reported by loading series of co-catalyst different from Pt) but much higher than almost all of the reported conjugated polymers [21–24,26,36,37,39,40]. Based on the above results and discussion, a
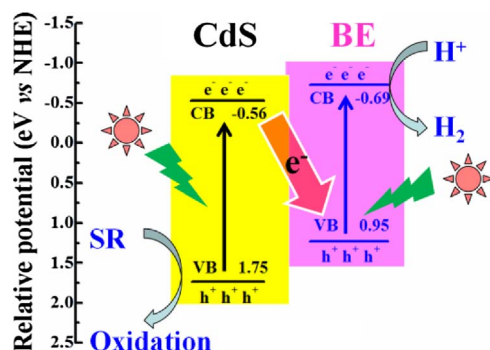
Fig. 10. Proposed photocatalytic H_2 production procedure according to Z-scheme electron transfer mechanism.

proposed mechanism for H_2 production over the present Z-scheme BE-CdS hybrid is shown in Fig. 10. Both BE and CdS can be excited to generate e^-/h^+ pairs under visible light irradiation, and then the e^- in CB of CdS can transfer to the VB of BE through Z-scheme mode. In this step, the e^-/h^+ separation efficiency of both BE and CdS can be improved. Finally, the assembling electrons on CB of BE participate in photocatalytic water reduction for H_2 production, and the h^+ on VB of CdS can be reduced by Na_2S/Na_2SO_3.

4. Conclusions

In summary, energy band engineering between inorganic (CdS) and organic (BE) semiconductors is successfully utilized to fabricated a Z-scheme BE-CdS hybrid photocatalyst for visible light driven H_2 production from water splitting. Band structure analysis reveals the favorable staggered energy band arrangement between BE and CdS, and the technique of in-situ photodeposition of Pt confirms the existence of Z-scheme electron transfer mode. Photocatalytic tests indicate that optimal H_2 production rate over BE-CdS hybrid is 8.3 and 23.3 times higher than that of CdS and BE respectively. And the extremely enhancement of photoactivity should be attributed to the broad vis/NIR light absorption ability and quick internal Z-scheme electron transfer, which is evidenced by DRS, PL, photocurrent and EIS characteristics. More importantly, wavelength dependent AQY curve reveals the BE-CdS hybrid can drive water splitting under the whole 400–700 nm vis/NIR light region. Especially, AQY values of 7.5% and 0.2% are obtained under 420 and 700 nm monochromatic light irradiation respectively. The present work gives a new route for designing high efficient semiconductor hybrid photocatalyst with broad absorption region as well as quick charge separation.

Acknowledgments

Appendix A. Supplementary data

Supplementary data associated with this article can be found, in the online version, at http://dx.doi.org/10.1016/j.apcatb.2017.11.038.

References

[1] I. Roger, M.A. Shipman, M.D. Symes, Nat. Rev. Chem. 1 (2017) 0003.
[2] J. Low, J. Yu, M. Jaroniec, S. Wageh, A.A. Al-Ghamdi, Adv. Mater. 29 (2017) 1601694.
[3] X. Zhang, T. Peng, S. Song, J. Mater. Chem. A 4 (2016) 2365–2402.
[4] J. Willkomm, K.L. Orchard, A. Reynal, E. Pastor, J.R. Durrant, E. Reisner, Chem. Soc. Rev. 45 (2016) 9–23.
[5] W.J. Ong, L.L. Tan, Y.H. Ng, S.T. Yong, S.T. Chai, Chem. Rev. 116 (2016) 7159–7329.
[6] X. Zou, Y. Zhang, Chem. Soc. Rev. 44 (2015) 5148–5180.
[7] Y. Xu, C. Zhang, L. Zhang, X. Zhang, H. Yao, J. Shi, Energy Environ. Sci. 9 (2016) 2410–2417.
[8] K. Zhang, L. Wang, J. Kim, M. Ma, G. Veerappan, C. Lee, L. Kong, H. Lee, J. Park, Energy Environ. Sci. 9 (2016) 499–503.
[9] Y. Zheng, Y. Jiao, Y. Zhu, Q. Cai, A. Vasileff, L.H. Li, Y. Han, Y. Chen, S.Z. Qiao, J. Am. Chem. Soc. 139 (2017) 3336–3339.
[10] Z. Zhang, J. Huang, Y. Fang, M. Zhang, K. Liu, B. Dong, Adv. Mater. 29 (2017) 1606688.
[11] S. Cao, J. Low, J. Yu, M. Jaroniec, Adv. Mater. 27 (2015) 2150–2176.
[12] P. Zhou, J. Yu, M. Jaroniec, Adv. Mater. 26 (2014) 4920–4935.
[13] S. Liu, F. Chen, S. Li, X. Peng, Y. Xiong, Appl. Catal. B: Environ. 211 (2017) 1–10.
[14] T. Di, B. Zhu, B. Cheng, J. Yu, J. Xu, J. Catal. 352 (2017) 532–541.
[15] X. Li, K. Xie, L. Song, M. Zhao, Z. Zhang, ACS Appl. Mater. Inter. 9 (2017) 24577–24583.
[16] F.Q. Zhou, J.C. Fan, Q.J. Xu, Y.L. Min, Appl. Catal. B: Environ. 201 (2017) 77–83.
[17] X. Wang, K. Maeda, A. Thomas, K. Takanabe, G. Xin, J.M. Carlsson, K. Domen, M. Antonietti, Nat. Mater. 8 (2009) 76–80.
[18] H.J. Hou, X.H. Zhang, D.K. Huang, X. Ding, S.Y. Wang, X.L. Yang, S.Q. Li, Y.G. Xiang, H. Chen, Appl. Catal. B: Environ. 203 (2017) 563–571.
[19] G. Zhang, Z.A. Lan, X. Wang, Angew. Chem. Int. Ed. 55 (2016) 15712–15727.
[20] V.S. Vyas, B.V. Lotsch, Nature 521 (2015) 41–42.
[21] P. Pati, G. Damas, L. Tian, D.L.A. Fernandes, L. Zhang, I.B. Pehlivan, T. Edvinsson, C.M. Araujo, H. Tian, Energy Environ. Sci. 10 (2017) 1372–7376.
[22] J. Chen, C.L. Dong, D. Zhao, Y.C. Huang, X. Wang, L. Samad, L. Dang, M. Shearer, S. Shen, L. Guo, Adv. Mater. 29 (2017) 1606198.
[23] R.S. Sprick, B. Bonillo, R. Clowes, P. Guiglion, N.J. Brownbill, B.J. Slater, F. Blanc, M.A. Zwijnenburg, D.J. Adams, A.I. Cooper, Angew. Chem. Int. Ed. 55 (2016) 1792–1796.
[24] C. Yang, B.C. Ma, L. Zhang, S. Lin, S. Ghasimi, K. Landfester, K.A. Zhang, X. Wang, Angew. Chem. Int. Ed. 55 (2016) 9202–9206.
[25] X.H. Zhang, X.P. Wang, J. Xiao, S.Y. Wang, D.K. Huang, X. Ding, Y.G. Xiang, H. Chen, J. Catal. 350 (2017) 64–71.
[26] Z. Sun, H. Zheng, J. Li, P. Du, Energy Environ. Sci. 8 (2015) 2668–2676.
[27] R.S. Sprick, J.X. Jiang, B. Bonillo, S. Ren, T. Ratvijitvech, P. Guiglion, M.A. Zwijnenburg, D.J. Adams, A.I. Cooper, J. Am. Chem. Soc. 137 (2015) 3265–3270.
[28] J. Ran, J. Yu, M. Jaroniec, Green Chem. 13 (2011) 2708–2713.
[29] X. Jiao, Z. Chen, X. Li, Y. Sun, S. Gao, W. Yan, C. Wang, Q. Zhang, Y. Lin, Y. Luo, Y. Xie, J. Am. Chem. Soc. 139 (2017) 7586–7594.
[30] D. Liu, J. Wang, X. Bai, R. Zong, Y. Zhu, Adv. Mater. 28 (2016) 7284–7290.
[31] Y. Wang, M.K. Bayazit, S.J.A. Moniz, Q. Ruan, C. Lau, N. Martsinovich, J. Tang, Energy Environ. Sci. 10 (2017) 1643–1651.
[32] M.Y. Ye, Z.H. Zhao, Z.F. Hu, L.Q. Liu, H.M. Ji, Z.R. Shen, T.Y. Ma, Angew. Chem. Int. Ed. 56 (2017) 8407–8411.
[33] X. Yang, Y. Xiang, Y. Qu, X. Ding, H. Chen, J. Catal. 345 (2017) 319–328.
[34] X. Zhang, T. Peng, L. Yu, R. Li, Q. Li, Z. Li, ACS Catal. 5 (2015) 504–510.
[35] B. Chai, T. Peng, J. Mao, K. Li, L. Zan, Phys. Chem. Chem. Phys. 14 (2012) 16745–16752.
[36] J. Ran, B. Zhu, S. Qiao, Angew. Chem. Int. Ed. 56 (2017) 10373–10377.
[37] J. Ran, G. Gao, F.T. Li, T.Y. Ma, A. Du, S.Z. Qiao, Nat. Commun. 8 (2017) 13907.
[38] K. Liu, X. Yan, P. Zou, Y. Wang, L. Dai, Catal. Commun. 58 (2015) 132–136.
[39] B. Ma, H. Xu, K. Lin, J. Li, H. Zhan, W. Liu, C. Li, ChemSusChem 9 (2016) 820–824.
[40] L. Li, Z. Cai, Q. Wu, W.Y. Lo, N. Zhang, L.X. Chen, L. Yu, J. Am. Chem. Soc. 138 (2016) 7681–7686.